Journal of Materials Science & Technology 35 (2019) 1825–1830

Contents lists available at ScienceDirect

Journal of Materials Science & Technology

journal homepage: www.jmst.org

Research Article

Thermally stable microstructures and mechanical properties of B_4C-Al composite with in-situ formed $Mg(Al)B_2$

Yangtao Zhou[a,1], Yuning Zan[a,1], Shijian Zheng[a,*], Xiaohong Shao[a], Qianqian Jin[a], Bo Zhang[a], Quanzhao Wang[b], Bolv Xiao[a], Xiuliang Ma[a,c], Zongyi Ma[a,*]

[a] Shenyang National Laboratory for Materials Science, Institute of Metal Research, Chinese Academy of Sciences, Shenyang 110016, China
[b] Key Laboratory of Nuclear Materials and Safety Assessment, Institute of Metal Research, Chinese Academy of Sciences, Shenyang 110016, China
[c] School of Materials Science and Engineering, Lanzhou University of Technology, Lanzhou 730050, China

ARTICLE INFO

Article history:
Received 29 March 2019
Received in revised form 12 April 2019
Accepted 19 April 2019
Available online 24 April 2019

Keywords:
B_4C-Al composites
Thermal stability
In-situ reinforcement
Grain boundaries
Solute segregation

ABSTRACT

B_4C particulate-reinforced 6061Al composite was fabricated by powder metallurgy method. The as-rolled composite possesses high tensile strength which is comparable to that of the peak-aged 6061Al alloy. More importantly, the microstructures and mechanical properties are thermally stable during long-term holding at elevated temperature (400 °C). The microstructual contributions to the strength of the composite were discussed. Transmission electron microscopy (TEM) analysis indicates that the in-situ formed reinforcement $Mg(Al)B_2$, as products of the interfacial reactions between B_4C and the aluminum matrix, show not only good resistance to thermal coarsening but also strong pinning effect to the grain boundaries in the alloy matrix.

1. Introduction

Due to the light weight, high strength, and particularly the neutron shielding property, B_4C particulate-reinforced aluminum matrix (B_4C-Al) composite has received wide attention in recent years [1–8]. The B_4C-Al thin plates are used as neutron absorber material (NAM) for transport and storage of spent nuclear fuels. In some cases, the materials may be exposed for long periods at elevated temperatures (>300 °C) caused by the accumulation of heat from the spent fuels. For economy and safety consideration, there has been a growing interest to develop light-weight B_4C-Al racks with higher storage capacity where the strength and thermal stability are both required for the NAM.

Generally, precipitate strengthening and grain refinement are basic strategies to improve the materials strength. For the commonly used aluminum matrix, however, rapid coarsening of precipitates and grains easily occurs at temperatures higher than 150 °C, resulting in the detrimental effects to mechanical properties. Alternatively, high cost Al-Sc-Zr alloy was used to fabricate the NAMs. Due to the outstanding thermal stability of the precipitates $Al_3(Sc, Zr)$ in the matrix, the composite did not loss the strength after 2000 h of annealing at 300 °C [9].

It is known that interfacial reactions between B_4C particles and the molten aluminum matrix can generate various reaction products depending on the alloying elements and reaction conditions [10–13]. The benefits of interfacial reactions include interface wetting and increasing adhesion between B_4C reinforcement and the aluminum matrix [14]. In our previous work [15], we reported that the MgB_2 dispersions in the aluminum matrix were generated via the chemical reactions between B_4C particles and alloying elements. As usual, the reaction products possess higher melting points and higher stability at the working temperature for a neutron absorber. Enlightened by this work, it is meaningful to know if the in-situ formed dispersoids can stabilize and strengthen the composites, in which case, a novel method without additional cost can be developed to fabricate the desired NAMs.

2. Experiments

The B_4C-Al composite was fabricated by powder metallurgy technique using 6061Al alloy with a nominal composition of Al-1.0Mg-0.65Si-0.25Cu (wt.%) as the matrix and B_4C particles with an average diameter of ~7 μm as the reinforcements (26 wt.%). The as-mixed Al and B_4C powders were cold compacted in a cylindrical die under a pressure of 50 MPa and then hot pressed at 630 °C

* Corresponding authors.
E-mail addresses: sjzheng@imr.ac.cn (S. Zheng), zyma@imr.ac.cn (Z. Ma).
[1] These authors contributed equally to this work.

https://doi.org/10.1016/j.jmst.2019.04.019
1005-0302/

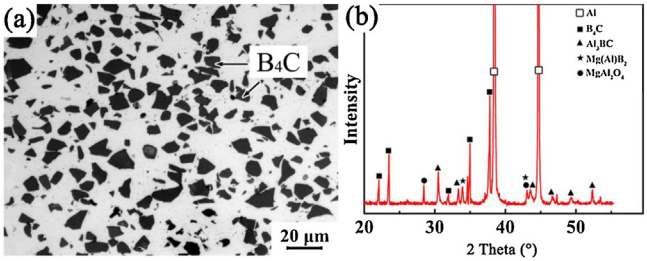

Fig. 1. (a) Optical micrograph of the B_4C-Al composite. The dark particles are B_4C reinforcement which shows uniform distribution. (b) XRD pattern of the composite. Besides Al and B_4C, Al_3BC and MgB_2 compounds can also be found.

under a pressure of 30 MPa for 2 h, producing the composite billets. Then the hot-pressed billets were hot-forged at 480 °C and rolled at 450 °C into plates. To evaluate the long-term thermal stability, the samples were annealed at an elevated temperature (400 °C) for various periods.

Electron back-scatter diffraction (EBSD) was used to characterize the grain size in the samples. These maps were achieved by using a field-emission scanning electron microscopy (Zeiss Supra 55). TEM experiments were carried out by a Tecnai F30 G^2 and a Titan G^2 60–300 aberration-corrected microscope. The microscopes are equipped with a high-angle annular dark-field (HAADF) detectors and X-ray energy dispersive spectrometer (EDS) systems. Since HAADF mode provides incoherent image which leads to strong atomic number (Z) contrast and is sensitive to the local chemical composition [16], the secondary phases with distinct compositions can be clearly seen.

Specimens for strength tests were machined from the composite sheets along the forging direction. Specimens with a gauge length of 15 mm, a width of 3 mm and a thickness of 2.5 mm were used. At least 5 tensile specimens were tested for each composite at a strain rate of 10^{-3}. Tests were conducted using Instron 8810.

3. Results and discussion

Fig. 1(a) shows the optical micrograph of the composite sample. The dark particles are B_4C which uniformly distribute in the alloy matrix and no micro-pores are observed. The XRD result is given in Fig. 1(b). The diffraction peaks of different phases are marked. Besides Al and B_4C, Al_3BC, MgB_2 and $MgAl_2O_4$ are also found.

Fig. 2 shows a HAADF image of a typical area in the specimen. The B_4C particles are well bonded with the aluminum matrix. At the B_4C/Al interface, an Al_3BC layer with thickness of ~0.3 μm is clear seen. In the alloy matrix, high dense nano-rods can be observed, as marked by arrows.

The nano-rods were characterized by TEM and EDS analysis. Fig. 3(a) and (b) show the bright-field (BF) TEM images of an individual nano-rod viewed along two perpendicular directions. The nano-rod possesses a hexagonal prism configuration. EDS and electron diffraction analysis were performed on the nano-rod along its long axis as shown in Fig. 3(c) and (d) to avoid interference from overlapped aluminum matrix. The results suggest that the nano-rod is $Mg(Al)B_2$ compound with a hcp lattice (a = 0.31 nm, c = 0.35 nm). According to the quantitative calculation based on EDS signals, the ratio of Mg:Al in this compound is about 1:1. Thus, it can be deduced that Al_3BC and $Mg(Al)B_2$ were generated by the chemical reactions between B_4C and the alloy matrix following the routes:

$$3Al + B_4C \rightarrow Al_3BC + 3B \quad (1)$$

$$2B + 0.5Mg + 0.5Al \rightarrow Mg(Al)B_2 \quad (2)$$

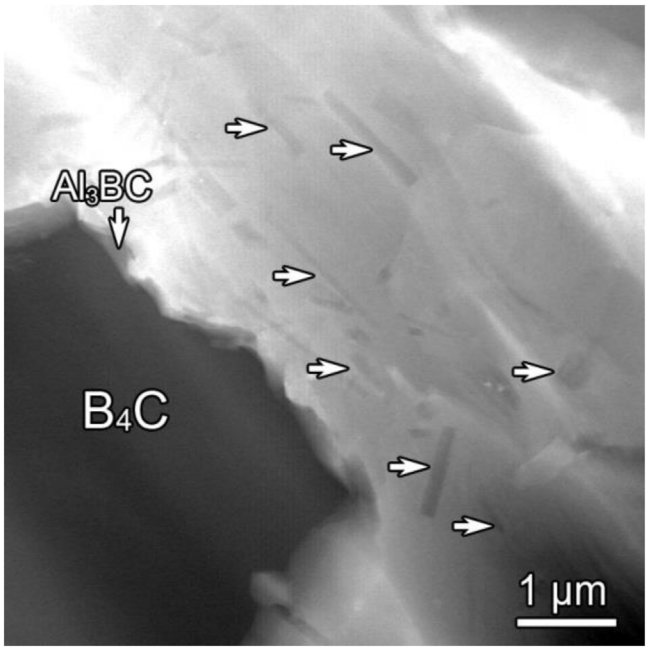

Fig. 2. HAADF image showing the microstructures in the B_4C-Al composite. Discontinuous Al_3BC particles are present at the B_4C/Al interface. High dense nano-rods as arrowed are observed in the alloy matrix.

To evaluate the mechanical properties of the composite, tensile tests were conducted. The stress-strain curve of the composite is shown in Fig. 4(a). The yield strength (YS) and the ultimate tensile strength (UTS) are 205 MPa and 315 MPa, respectively. It is seen that the UTS of the composite is comparable to that of the peak-aged commercial 6061Al alloy [17], although the YS is a little lower. Being distinct with the aged aluminum alloy, the mechanical properties of the composite is quite thermally stable. As seen in Fig. 4(b), the composite maintained the same strength level even after 8000 h of exposure at the elevated temperature of 400 °C.

The stable mechanical properties originated from the structural stability in the material. We then characterized the microstructures of the composite experienced long-term annealing. Due to the low reactivity between B_4C and aluminum, we did not find any obvious change for the B_4C particles in the annealed samples. Attention was paid to the in-situ formed $Mg(Al)B_2$ reinforcement. The lengths and diameters of the $Mg(Al)B_2$ nano-rods in the samples after various aging durations were statistically measured. The results are given in Fig. 5. The size distribution of the $Mg(Al)B_2$ remained almost unchanged even after 8000 h of thermal exposure, indicating its excellent stability at the elevated temperature.

More interestingly, the alloy grains in the composite were also thermally stable against coarsening during the long-term annealing. Fig. 6(a) is the EBSD map of the as-rolled sample, showing a fine grained microstructure generated by forging and rolling process. In this map, red lines denote the high-angle grain boundaries (GBs) with misorientation angles larger than 15°, whereas the black lines are the low-angle GBs with misorientation angles in between 5°–15°. It is seen that most of the GBs present high misorientation angles. Based on Fig. 6(a), an average grain size can be measured to be 1.8 μm. The EBSD map of the sample experienced 8000 h annealing is shown in Fig. 6(b). The grains in this composite did not grow evidently except small reduction of low angle GBs. Statistical measurements suggested the average grain size still remained as 2.5 μm.

For particulate-reinforced aluminum composite, the strengthening mechanisms provided by B_4C particles include load transfer (L–T) and geometrically necessary dislocations (GNDs). The shear

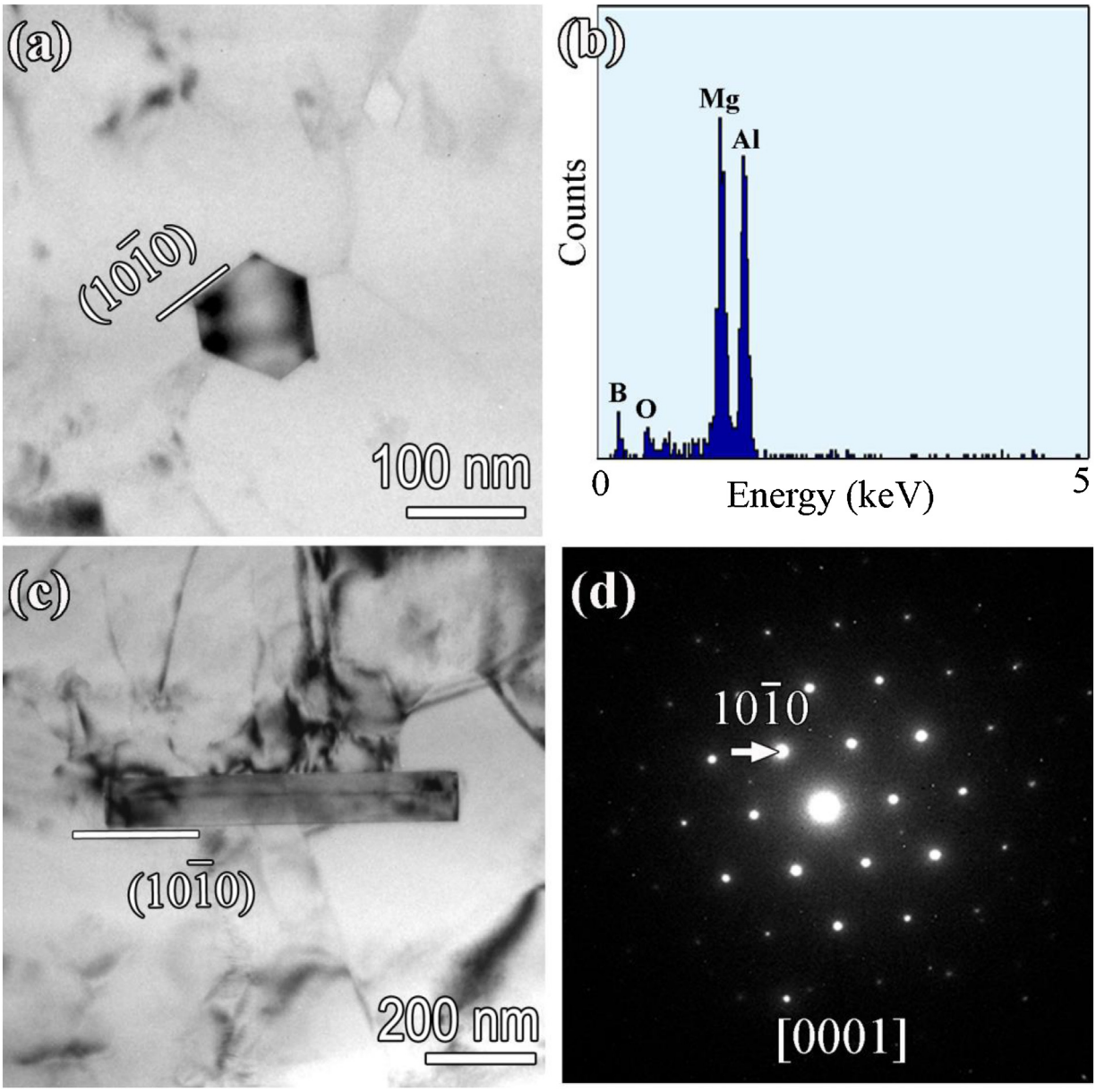

Fig. 3. TEM analysis on the Mg(Al)B_2 nano-rods. (a) and (b) bright-field TEM images of the nano-rod viewed along two perpendicular directions. (c) EDS profile indicates the nano-rod is composed of Mg, Al and B. (d) SAED pattern of the compound along its [0001] zone axis.

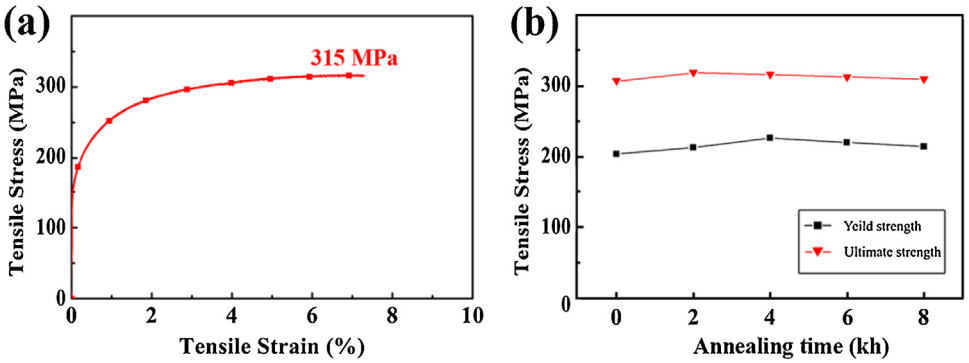

Fig. 4. (a) Stress–strain curve of the composite from tensile tests. (b) The values of yield strength and ultimate strength of the composite experienced various annealing periods. The composite shows high stability after the exposure to elevated temperature.

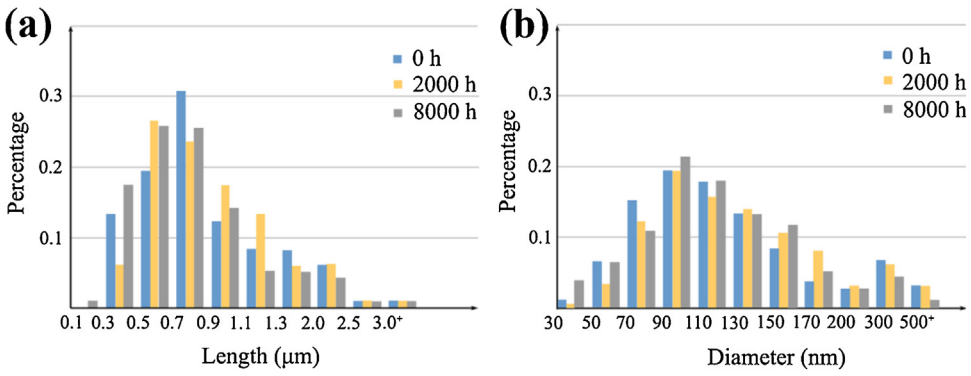

Fig. 5. Distribution of the lengths and diameters of the Mg(Al)B_2 nano-rods suffered various periods of high temperature exposure.

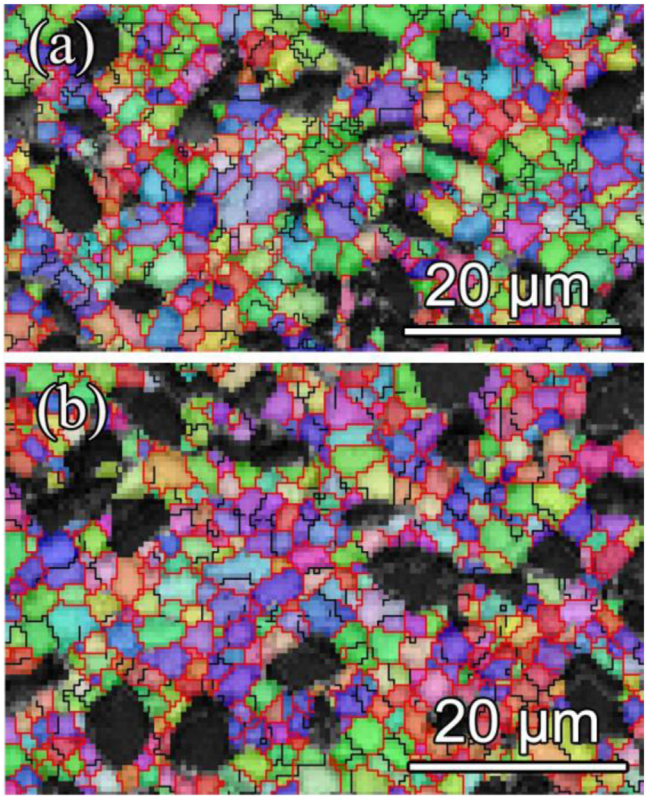

Fig. 6. (a) EBSD map of the grain structures in the as-rolled sample. (b) The matrix grains in the sample experienced thermal exposure for 8000 h. Equiaxed grains with an average diameter of ~2.5 μm are observed.

lag theory [18] is usually used to estimate the tensile transfer of load from the matrix to the discontinuous reinforcement. The strength contribution from the reinforcement with volume fraction 'Vp' and aspect ratio 's' is given by

$$\Delta\sigma_{LT}=\frac{\sigma_0 \cdot V_p \cdot (s+2)}{2}$$

where 'σ_0' is the yield strength of the alloy matrix (~80 MPa for 6061Al [17]). The volume fraction of B_4C in the present composite is ~0.27.

The GNDs are formed due to the incompatibility in the elastic modulus of B_4C and Al [19]. The strengthening effect can be calculated by

$$\Delta\sigma_d=\alpha\mu b\sqrt{\frac{8V_p\varepsilon_y}{bD_B}}$$

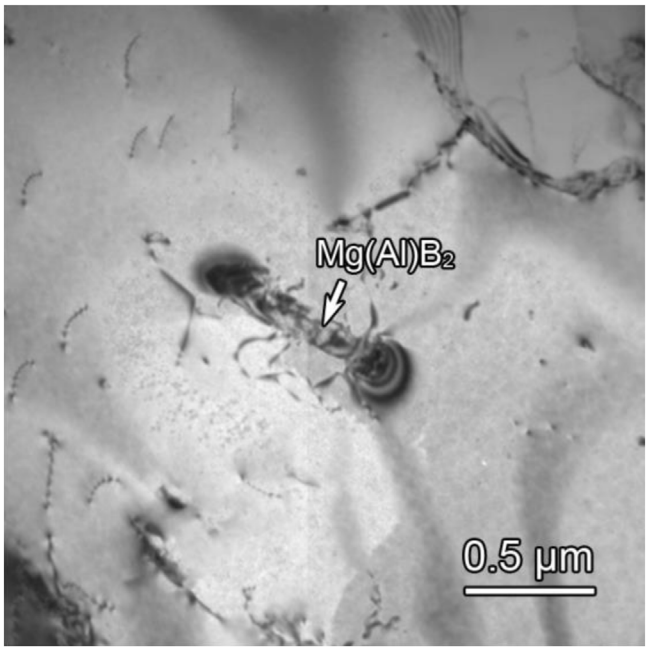

Fig. 7. Bright-field TEM image of a Mg(Al)B_2 nano-rod in the deformed sample. At both ends of the rod, the black contrast indicates the high strain state in the alloy matrix nearby. The dislocation lines are also clear seen around the nano-rod.

where α = 1.25, 'μ' is the shear modulus (~27 GPa) and 'b' is the Burger vector of a dislocation in aluminium. 'D_B' is the average diameter of B_4C particles.

The strengthening effect also comes from Mg(Al)B_2 nano-rods. Fig. 7 shows a BF TEM image of a Mg(Al)B_2 nano-rod in the deformed sample. The fringe contrast on both ends of the rod indicates the high strain state at the places. It definitely shows the transfer of tensile load from the matrix to the nano-rod. Therefore, load bearing effect can be used to accounts for the extra strength provide by Mg(Al)B_2. On the other hand, dislocation lines tangled around the Mg(Al)B_2 nano-rod suggests the Orowan strengthening. The by-passing stress for a rod-shaped precipitate is [20]:

$$\Delta\sigma_{Orw}=2\left(\frac{\mu b}{4\pi\sqrt{1-\upsilon}}\right)\left[\frac{1}{\left(1.075\sqrt{0.433\pi/f}-\sqrt{1.732}\right)D_M}\right]\left(\ln\frac{\sqrt{1.732}D_M}{r_0}\right)$$

where 'υ' is Poisson's ratio (0.34), 'f' and 'D_M' are volume fraction and average diameter of Mg(Al)B_2 (~110 nm), respectively.

In addition, the Hall-Petch strengthening arose from the grain refinement is estimated by the relationship:

$$\Delta\sigma_{HP}=k_y d^{-1/2}$$

Table 1
Estimated contributions to the YS of the composite from different strengthening mechanisms.

	L-T (B_4C)	GNS	Hall-Petch	L-T ($Mg(Al)B_2$)	Orowan
YS increase (MPa)	32	17	42	11	17

where 'k_y' is ~0.06 MPa $m^{1/2}$ for pure Al [21] and should be a little larger for Al alloys. 'd' is average grain size estimated from EBSD analysis.

The improvement of the composite strength induced by the above factors is given in Table 1. By linear summation of the contributions from each mechanism, we got the simultaneously enhanced strength being ~119 MPa, which agreed well with the experimental result. It is seen that over 70% enhancement in yield strength of the composite comes from the contribution of B_4C reinforcement and grain refinement. The interfacial reaction products $Mg(Al)B_2$ add a relatively small portion. However, the nano-rods play an important role in the thermal stability of the composite.

Firstly, being different with the common strengthening precipitates in aluminium alloys, $Mg(Al)B_2$ is highly stable at the annealing temperature [22]. According to the statistic measurement shown in Fig. 5, the $Mg(Al)B_2$ did not grow up even after 8000 h of annealing. It retains the strengthening effect.

Besides the stability of the boride itself, the benefits of the nano-rods also lie in their pinning effect against the grain coarsening. Fig. 8 is a HAADF image taken from the annealed sample. The dot lines are depicted along the GBs. At the boundaries and triple junctions, as arrowed, we can find several $Mg(Al)B_2$ nano-rods. It evidently shows that the GB migration was impeded by the dispersive nano-rods.

Moreover, we noted that the GBs connecting with $Mg(Al)B_2$ particles always showed bright contrast which implied that these boundaries probably contained different chemical compositions. Therefore, EDS mapping was performed on the GB connecting to a $Mg(Al)B_2$ particle. To ensure the accuracy of the compositional analysis, a nearly edge-on GB was selected. Fig. 9(a) shows a HAADF image and the elemental mapping of the area framed with a red box. The result demonstrates the enrichment of Cu at the $Mg(Al)B_2$/Al interface and the GB nearby. Also, the scenario was confirmed by the high-resolution HAADF imaging. The atomic structure of the $Mg(Al)B_2$/Al interface is displayed in Fig. 9(b). A nearly 2 nm-thick layer is observed in the Al matrix adjacent to $Mg(Al)B_2$. The bright contrast indicates the copper enrichment. The copper segregated layer at the $Mg(Al)B_2$/Al interfaces has also been detected in the as-received sample but with thickness less than 1 nm [15]. It suggests that the long-term ageing enhanced segregation of Cu at the interface areas. Fig. 9(c) shows a high-magnification HAADF image of the GB where the bright contrast with 0.5 nm in thickness indicates the Cu segregation. The Cu concentration gradually decreases in the GB from the region close to the $Mg(Al)B_2$ to that away from it. It suggests that the Cu atoms in the GB should spring from the $Mg(Al)B_2$/Al interfaces. Close inspection on the GB indicates the solute atoms formed a cluster-like pattern, but no well-defined precipitate can be observed.

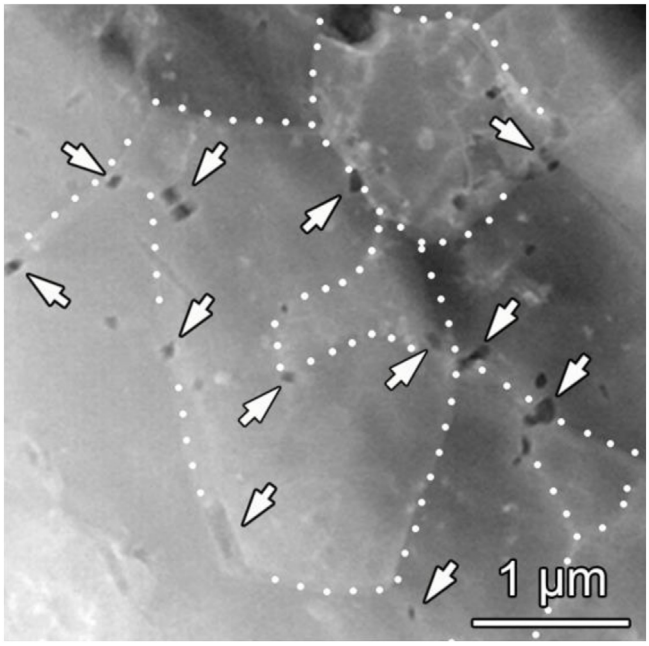

Fig. 8. HAADF image showing that the grain boundaries are pinned by the $Mg(Al)B_2$ dispersoids in the sample annealed for 8000 h.

The stabilizing effect of $Mg(Al)B_2$ to GBs is well known as Zener pinning. In a particle containing alloy, the maximum grain size can be simply estimated by $d=D_M/0.75f$, where 'D_M' is the size and 'f' is the volume fraction of particles, respectively [23]. Simply taking the effect of $Mg(Al)B_2$ into account, the stable grain size can be reduced to ~3.7 μm. Furthermore, we propose that the solute Cu segregation can provide extra stabilizing effect to GBs: as a GB has been pinned by the $Mg(Al)B_2$ nanorod, the Cu atoms around $Mg(Al)B_2$ are prone to diffuse along the GB since it provides a low-

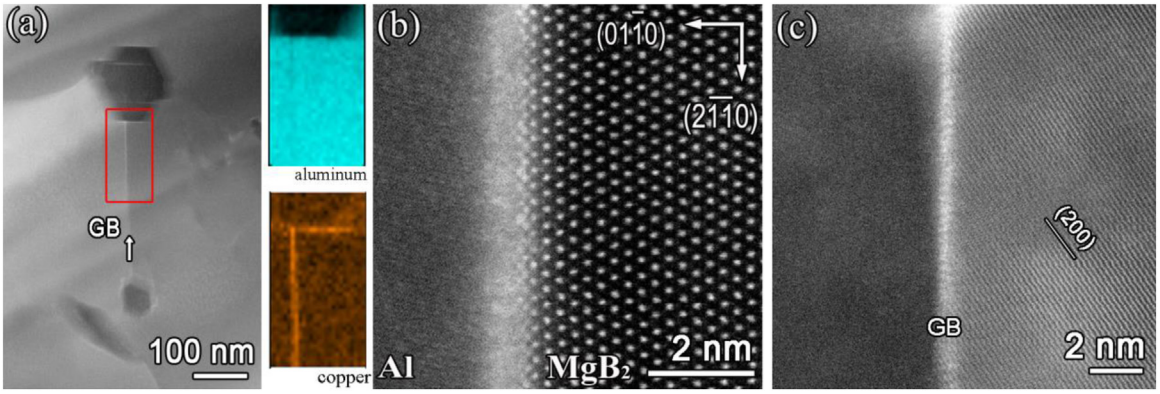

Fig. 9. (a) A HAADF image and EDS mapping showing the Cu distribution at the $Mg(Al)B_2$/Al interface and along the grain boundary. (b) High resolution HAADF image of the Cu-segregated $Mg(Al)B_2$/Al interface. (c) HAADF image of the grain boundary. High concentration of Cu atoms is observed in the boundary close to the $Mg(Al)B_2$ particle.

energy path for Cu diffusion. According to the simulation performed on some typical Al GBs, the Cu segregation could decrease the GB energy due to the creation of new Cu-Al bonds across the boundary [24,25]. The migration of a Cu-contained GB requires breakdown of the Cu-Al bonds and transport of Cu atoms along with the migrating boundary [26]. In consequence, this drag effect leads to an obviously lower mobility of GBs even under thermal annealing.

4. Conclusion

In the present work, a B_4C/Al composite was fabricated by powder metallurgy method. The composite possessed high strength and importantly thermal stability at elevated temperatures. Theoretical estimation indicated that the B_4C reinforcement, grain refinement and the in-situ formed Mg(Al)B_2 contributed to the increased strength when compared to the matrix alloy. The thermal stability of the composite was mainly due to the thermally stable Mg(Al)B_2 compound. The dispersive Mg(Al)B_2 nano-rods showed good resistance to coarsening and also stabilized the alloy grains by Zener pinning effect. Moreover, the solute Cu atoms segregating at Mg(Al)B_2/Al interfaces tended to diffuse along grain boundaries and further lowered the grain boundary mobility.

Acknowledgements

This work was supported by the National Natural Science Foundation of China (grant numbers U1508216, 51501195, 51771194, 51771201), and Liaoning Province (20180551101) and the Innovation Fund of IMR (2017-PY10). S.J.Z acknowledges 'Thousand Youth Talents Plan' of China. Thanks to Mr. B. Wu and L.X. Yang for their technical support in TEM, and to C.L. Jia for his help in EBSD.

References

[1] X.-G. Chen, in: N. Gupta, W.H. Hunt (Eds.), Solidification Processing of Metal Matrix Composites, TMS, USA, 2006, pp. 343–350.
[2] P. Zhang, Y. Li, W. Wang, Z. Gao, B. Wang, J. Nucl. Mater. 437 (2013) 350–358.
[3] X.-G. Chen, L. St-Georges, M. Roux, Mater. Sci. Forum 706–709 (2012) 631–637.
[4] X. Yue, J. Wang, Y. Li, H. Ru, Mater. Res. Bull. 48 (2013) 1720–1724.
[5] H.S. Chen, W.X. Wang, Y.L. Li, P. Zhang, H.H. Nie, Q.C. Wu, J. Alloys Compd. 632 (2015) 23–29.
[6] L. Zhou, C. Cui, Q.Z. Wang, C. Li, B.L. Xiao, Z.Y. Ma, J. Mater. Sci. Technol. 34 (2018) 1730–1738.
[7] N.H. Tariq, L. Gyansah, X. Qiu, C. Jia, H.B. Awais, C. Zheng, H. Du, J. Wang, T. Xiong, J. Mater. Sci. Technol. 35 (2019) 1053–1063.
[8] M. Gao, Z. Chen, H. Kang, E. Guo, R. Li, Y. Fu, H. Xie, T. Wang, J. Mater. Sci. Technol. 35 (2019) 1523–1531.
[9] J. Lai, Z. Zhang, X.-G. Chen, Mater. Sci. Eng. A 532 (2012) 462–470.
[10] Z. Luo, Y. Song, S. Zhang, D.J. Miller, Metall. Mater. Trans. A 43 (2011) 281–293.
[11] J. Lai, Z. Zhang, X.-G. Chen, J. Mater. Sci. 46 (2011) 451–459.
[12] K.B. Lee, H.S. Sim, S.Y. Cho, H. Kwon, Mater. Sci. Eng. A 302 (2001) 227–234.
[13] Y.Z. Li, Q.Z. Wang, W.G. Wang, B.L. Xiao, Z.Y. Ma, Mater. Chem. Phys. 154 (2015) 107–117.
[14] M. Kubota, J. Alloys Compd. 504S (2010) S319–S322.
[15] Y.T. Zhou, Y.N. Zan, S.J. Zheng, Q.Z. Wang, B.L. Xiao, X.L. Ma, Z.Y. Ma, J. Alloys Compd. 728 (2017) 112–117.
[16] S.J. Pennycook, Adv. Imag. Elect. Phys. 123 (2002) 173–206.
[17] F. Ozturk, A. Sisman, S. Toros, S. Kilic, R.C. Picu, Mater. Des. 31 (2010) 972–975.
[18] V.C. Nardone, K.M. Prewo, Scr. Metall. Mater. 20 (1986) 43–48.
[19] F. Tang, I.E. Anderson, T. Gnaupel-Herold, H. Prask, Mater. Sci. Eng. A 383 (2004) 362–373.
[20] J.F. Nie, B.C. Muddle, I.J. Polmear, Mater. Sci. Forum 217–222 (1996) 1257–1262.
[21] S. Thangaraju, M. Heilmaier, B.S. Murty, S.S. Vadlamani, Adv. Eng. Mater. 14 (2012) 892–897.
[22] G.K. Moiseev, A.L. Ivanovskii, Inorg. Mater. 41 (2005) 1061–1066.
[23] V.L. Tellkamp, A. Melmed, E.J. Lavernia, Metall. Mater. Trans. A 32 (2001) 2335–2343.
[24] D. Zhao, O.M. Løvvik, K. Marthinsen, Y. Li, Acta Mater. 145 (2018) 235–246.
[25] M. Muzyk, K.J. Kurzydlowski, Mater. Res. Soc. Symp. Proc. 1297 (2011) 155–159.
[26] M.I. Mendelev, D.J. Srolovitz, Modelling Simul. Mater. Sci. Eng. 10 (2002) R79–R109.